Nanoscale

ROYAL SOCIETY OF CHEMISTRY

PAPER

View Article Online
View Journal | View Issue

Check for updates

Cite this: *Nanoscale*, 2020, **12**, 3965

An as-cast high-entropy alloy with remarkable mechanical properties strengthened by nanometer precipitates

Gang Qin,[a] Ruirun Chen, *[a] Peter K. Liaw,[b] Yanfei Gao,[b] Liang Wang,[a] Yanqing Su,[a] Hongsheng Ding,[a] Jingjie Guo[a] and Xiaoqing Li[c]

Received 27th September 2019,
Accepted 2nd January 2020

DOI: 10.1039/c9nr08338c

rsc.li/nanoscale

High-entropy alloys (HEAs) with good ductility and high strength are usually prepared by a combination of forging and heat-treatment processes. In comparison, the as-cast HEAs typically do not reach strengths similar to those of HEAs produced by the forging and heat-treatment processes. Here we report a novel equiatomic-ratio CoCrCuMnNi HEA prepared by vacuum arc melting. We observe that this HEA has excellent mechanical properties, *i.e.*, a yield strength of 458 MPa, and an ultimate tensile strength of 742 MPa with an elongation of 40%. Many nanometer precipitates (5–50 nm in size) and domains (5–10 nm in size) are found in the inter-dendrite and dendrite zones of the produced HEA, which is the key factor for its excellent mechanical properties. The enthalpy of mixing between Cu and Mn, Cr, Co, or Ni is higher than those of mixing between any two of Cr, Co, Ni and Mn, which leads to the separation of Cu from the CoCrCuMnNi HEA. Furthermore, we reveal the nanoscale-precipitate-phase-forming mechanism in the proposed HEA.

Introduction

High-entropy alloys (HEAs) composed of more than four multiple principal elements have attracted significant research interest owing to their appealing properties,[1–23] since they were first reported in 2004.[24,25] Although the principal elements in the HEAs have different crystal structures, often HEAs exhibit simple solid-solution phases, *i.e.*, body-centered-cubic (BCC), face-centered-cubic (FCC), and hexagonal-close-packed structures. The concept of HEAs has seen a significant development in the field of alloy design, and it opens up a door to explore new high-performance materials.

To find high-performance HEAs, many investigations on the magnetic properties, and mechanical properties at different temperatures, and microstructures of HEAs were carried out.[1,3,6,26–31] So far, some HEAs with remarkable mechanical performances were designed.[1,3,6,26,32–49] For example, a metastable dual-phase HEA that exhibits an excellent strength-ductility combination due to the transformation-induced plasticity effects was proposed by Li *et al.*[26] Gludovatz *et al.* discovered that the five-element high-entropy alloy, CrMnFeCoNi,[49] has exceptional damage tolerance, and its tensile strength and fracture toughness are above 1 GPa and 200 MPa·m$^{1/2}$, respectively, at a cryogenic temperature.[49] They found that the main factor for the enhanced properties at cryogenic temperatures is the formation of the deformation nanotwinning.[49] Yang *et al.* proposed a HEA with a tensile strength of 1.5 GPa and a tensile strain of 50% at ambient temperature by introducing high-density intermetallic nanoparticles.[32] Fu *et al.* designed an FCC single-phase nano-crystalline $Co_{25}Ni_{25}Fe_{25}Al_{7.5}Cu_{17.5}$ HEA.[37] The bulk HEA has an ultra-high compressive yield strength, which is higher than that of any FCC HEA reported in the previous literature.[37] They claimed that grain-boundary strengthening and dislocation strengthening are principally responsible for the measured ultra-high strength of the HEA.[37]

3d Transition metals (*e.g.*, Mn, Fe, Co, Cr, Ni, and Cu) were frequently used to form alloy systems in the field of HEAs. According to the principle of permutation and combination, six kinds of equi-molar HEAs that contain five principal elements can be formed with these elements, for example, CoCrCuFeNi,[38,39] CoCrFeMnNi,[40,41] CoCuFeMnNi,[42] CrCuFeMnNi,[33] and CoCrCuFeMn.[44] These five HEAs have been studied in recent years.[38–44] However, no information on the CoCrCuMnNi HEA is obtained. Furthermore, the reported HEAs with good ductility and high strength were usually

[a]*National Key Laboratory for Precision Hot Processing of Metals, Harbin Institute of Technology, 150001, China. E-mail: ruirunchen@hit.edu.cn; Fax: +86-451-86412394; Tel: +86-451-86412394*
[b]*Department of Materials Science and Engineering, The University of Tennessee, Knoxville, TN 37996, USA*
[c]*Department of Materials Science and Engineering, KTH - Royal Institute of Technology, 10044 Stockholm, Sweden*

treated by rolling, heat treatment, and so on,[1,3,6,26,32–37,49] whereas HEAs prepared by direct casting rarely possess a good combination of high strength and large elongation. Here, to fill these gaps, we proposed the CoCrCuMnNi HEA that was obtained by vacuum arc melting. The phase composition, microstructure, and mechanical behavior of the equimolar CoCrCuMnNi HEA were studied. Moreover, the solid-solution strengthening was estimated to analyze the strengthening mechanisms in the proposed HEA. Finally, an atomic-diffusion model was used to describe the phase-forming process.

Experimental

An equi-atomic ratio CoCrCuMnNi HEA was prepared using an arc-melting technology in a high-purity argon atmosphere state. Metals with purity higher than 99 weight percent (wt%) were selected as raw materials. For improving the chemical homogeneity, the ingot was melted seven times. The phase structure of the HEA was identified by X-ray diffraction (XRD) using Cu Kα radiation (MXP21VAHF) from 20 to 100 degrees in 2θ at a scanning rate of 4 degrees per min. The microstructure of the specimen was characterized by scanning-electron microscopy (SEM) and transmission electron microscopy (TEM). The elemental distribution was determined by using an energy-dispersive spectrometer (EDS). For observing the microstructure, samples were ground and electro-polished (under a room-temperature condition, with an applied voltage of 27 V, the time is 15 s, and the electrolyte is a mixture of 90% acetic and 10% perchloric acid). Flat specimens (1 mm in thickness, 10 mm in the gauge length, and 2 mm in width) were used for tensile testing with an AG-X 20 kN electronic universal material testing machine at room temperature. The strain rate is 0.6 mm min^{-1}. The strain was measured using an extensometer.

Results

The tensile engineering stress–strain curve of the proposed CoCrCuMnNi HEA is presented in Fig. 1a. The obtained tensile yield and ultimate tensile strengths are about 458 MPa and 742 MPa, respectively, and the corresponding elongation is about 40%. To emphasize the substantial improvement in the mechanical properties of our proposed HEA, we compare our obtained results to those of some classical HEAs,[7,15,16,19,21,22,26,45–52,77–81] as shown in Fig. 1b–d. The corresponding values are listed in Table 1. It is evident that the CoCrCuMnNi HEA with an FCC structure possesses a good combination of strength and ductility, relative to other HEAs. It has a similar mechanical response to the single-phase $Fe_{20}Mn_{20}Ni_{20}Co_{20}Cr_{20}$ HEA (grain-refined)[49] and the dual-phase $Fe_{50}Mn_{30}Co_{10}Cr_{10}$ HEA (as-homogenized),[26] the two most successful HEAs to date.[26,49]

The XRD pattern of the CoCrCuMnNi HEA is presented in Fig. 2. Only two similar diffraction peaks are observed, which correspond to the FCC crystal structure. The reflection angles of the two peaks are similar, implying that they have a similar crystal structure. Moreover, the elemental distribution between the dendritic and inter-dendritic areas was inspected by EDS.

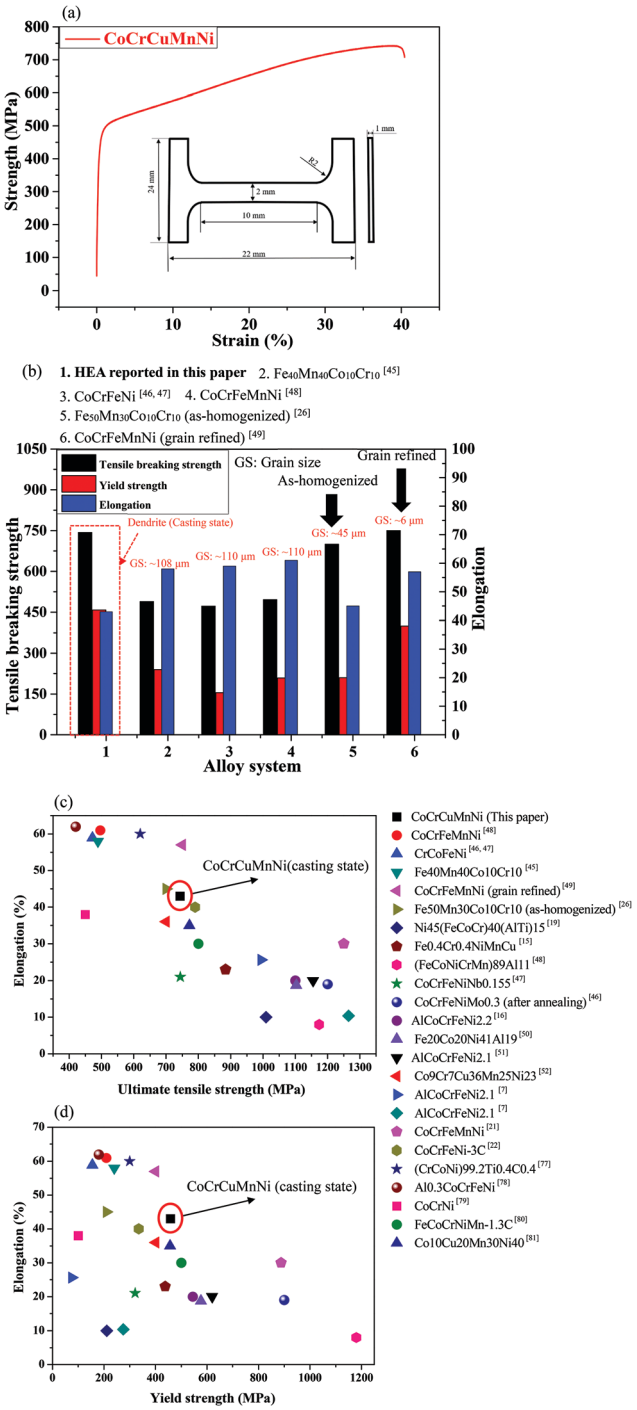

Fig. 1 Mechanical properties of the CoCrCuMnNi high-entropy alloy. (a) Tensile engineering stress–strain curves of the as-cast CoCrCuMnNi HEA. (b) Mechanical properties for different HEAs.[26,45–52] (c) The ultimate tensile strength and elongation for the CoCrCuMnNi HEA and other HEAs. (d) The tensile yield strength and elongation for the CoCrCuMnNi HEA and other HEAs.[7,15,16,19,21,22,26,45–52,77–81] The processing and heat-treatment conditions of these HEAs are shown in Table 1.

Table 1 Tensile mechanical properties of different HEAs[7,15,16,19,21,22,26,45–52,77–81]

HEA	Yield strength (MPa)	Ultimate tensile strength (MPa)	Elongation (%)	Condition
CoCrCuMnNi (this paper)	458	742	40	Casting
CoCrFeMnNi[48]	209	496	61	Casting
CrCoFeNi[46,47]	155	472	58.9	Casting
$Fe_{40}Mn_{40}Co_{10}Cr_{10}$[45]	240	489	58	Casting
CoCrFeMnNi (grain refined)[49]	400	750	57	Forging ~6 μm grains
$Fe_{50}Mn_{30}Co_{10}Cr_{10}$ (as-homogenized)[26]	210	700	45	Homogenized at 1200 °C for 2 h
$Ni_{45}(FeCoCr)_{40}(AlTi)_{15}$[19]	811	1009	10	Casting
$Fe_{0.4}Cr_{0.4}NiMnCu$[15]	438	884	23	Casting
$(FeCoNiCrMn)_{89}Al_{11}$[48]	1180	1174	8	Casting
$CoCrFeNiNb_{0.155}$[47]	321	744	21	Casting
$CoCrFeNiMo_{0.3}$[46] (after annealing)	900	1200	19	Annealed at 500 °C for 4 h
$AlCoCrFeNi_{2.2}$[16]	545	1100	20	Casting
$Fe_{20}Co_{20}Ni_{41}Al_{19}$[50]	577	1103	18.7	Casting
$AlCoCrFeNi_{2.1}$[51]	620	1155	20	Casting
$Co_9Cr_7Cu_{36}Mn_{25}Ni_{23}$[52]	401	700	36	Casting
$AlCoCrFeNi_{2.1}$[7]	75	994	25.6	Casting
$AlCoCrFeNi_{2.1}$[7]	275	1265	10.4	Cold rolling
CoCrFeMnNi[21]	888	1250	30	Forging and rolling ~6 μm grains
CoCrFeNi-3C[22]	335	790	40	Casting
$(CrCoNi)_{99.2}Ti_{0.4}C_{0.4}$[77]	300	620	60	Casting
$Al_{0.3}CoCrFeNi$[78]	180	420	62	Annealed at heat treatment 1250 °C for 2 h
CoCrNi[79]	100	450	38	Casting
FeCoCrNiMn-1.3C[80]	500	800	30	Casting
$Co_{10}Cu_{20}Mn_{30}Ni_{40}$[81]	457	772	35	Annealed at 1250 °C for 10 min

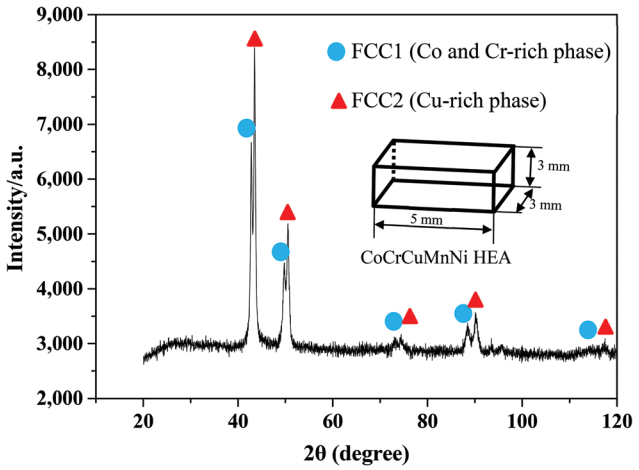

Fig. 2 XRD patterns of the CoCrCuMnNi high-entropy alloy.

It shows that the dendritic segregation areas are rich in Co and Cr, while inter-dendritic segregation areas are rich in Cu and Mn. The distribution of Ni is essentially identical. The skewing of the diffraction peaks could be caused by different lattice constants resulting from various elemental distributions between FCC1 and FCC2 structures.

Fig. 3a displays the SEM images of the CoCrCuMnNi HEA. It was found that the produced CoCrCuMnNi HEA has a typical dendrite crystal structure. Fig. 3b shows an image of the dendrite and inter-dendrite zones. Some plate-strip precipitates were observed in the inter-dendrite zone. Fig. 3c shows an image of the inter-dendrite zone with a high magnification. A mass of nanometer precipitates was found in the inter-dendrite zone. An image of the dendrite zone with high magnification is presented in Fig. 3d. In the dendrite zone, many nanometer precipitates were also observed.

For identifying the compositions of FCC1 and FCC2, EDS was applied in the HEA sample, and the results are shown in Fig. 4. It shows that the dendrite region is enriched with Cr and Co, and the inter-dendrite region is enriched with Cu.

To observe the nanostructure more clearly, the sample was analyzed by TEM. As shown in Fig. 5a, some nanometer-scale plate-strip precipitates (5–50 nm in size) were clearly observed. The interface between the matrix and precipitate is presented in Fig. 5b. Fig. 5c and d indicate that some nanometer precipitates (5–50 nm in size) were formed in this HEA. Fig. 5e shows the high-resolution TEM image for the dendrite zone. In the inter-dendrite zone, many nano-scale domains (5–10 nm in size) were observed. The selected-area diffraction (SAD) patterns are displayed in Fig. 5f. It shows that the dendrite has an FCC structure. Furthermore, the elemental-distribution maps of the nanometer precipitates show that these nanometer precipitates are Cu-rich, as shown in Fig. 6. Fig. 5g and h present the nanometer precipitates and their corresponding selected-area diffraction (SAD), which indicates that the nanometer precipitates possess an FCC structure. Fig. 5i presents the high resolution transmission electron microscopy (HRTEM) image of this HEA. It shows that the matrix and precipitates have a coherent relation at the interface. Fig. 5j and k present the HRTEM image of the nanometer precipitate and matrix, respectively. The lattice misfit ε between the matrix and nano-precipitate was estimated to be ~0.22% using the equation $\varepsilon = 2|d_1 - d_2|/(d_1 + d_2)$. Here d_1 and d_2 determined from the HRTEM micrographs are the interatomic distances

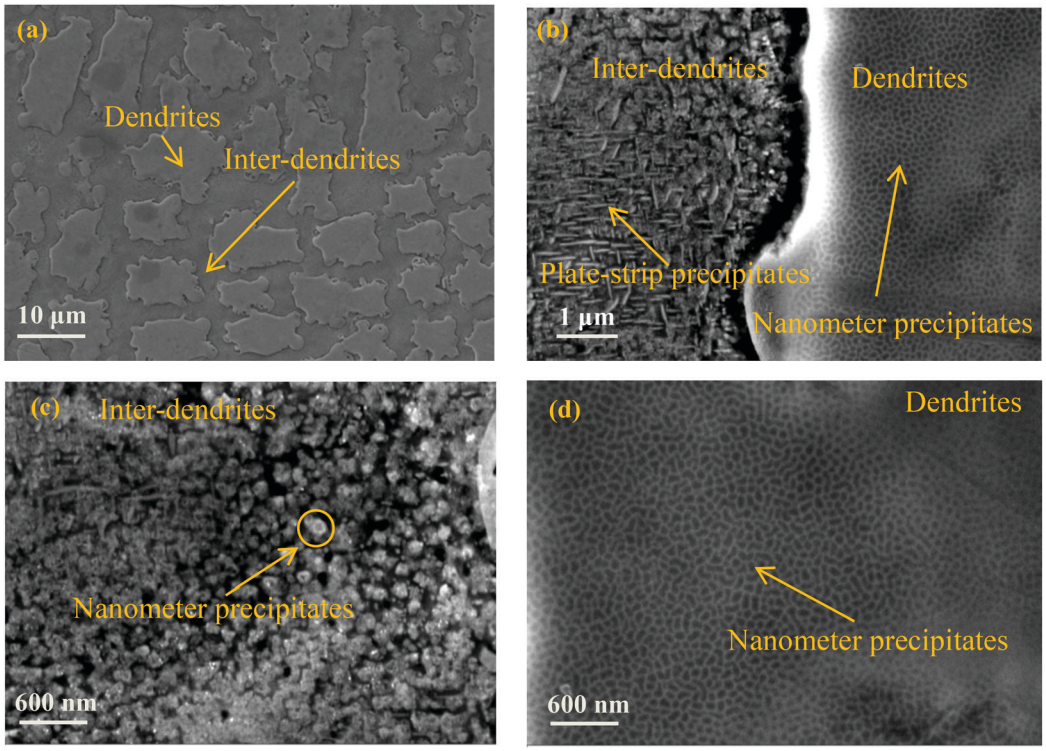

Fig. 3 SEM micrographs of the CoCrCuMnNi high-entropy alloy. (a) Image of the CoCrCuMnNi HEA. (b) Images of the dendrite and inter-dendrite zones. (c) Image of the inter-dendrite zone. (d) Image of the dendrite zone.

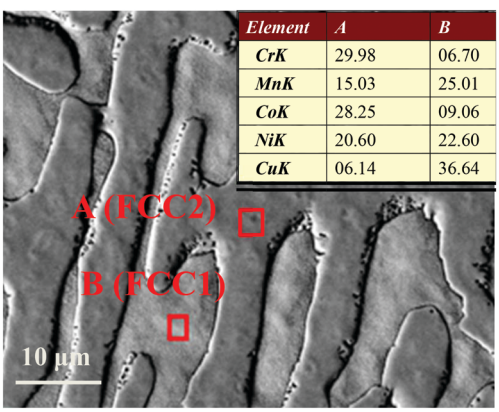

Element	A	B
CrK	29.98	06.70
MnK	15.03	25.01
CoK	28.25	09.06
NiK	20.60	22.60
CuK	06.14	36.64

Fig. 4 EDS results of the dendrite (marked A) and inter-dendrite region (marked B).

of {112} planes for the nano-precipitate and the matrix (see Fig. 5j and k), respectively.

Discussion

So far, some physical parameters were reported to discuss the phase formation and structural stability in HEAs,[50–64] such as the melting point T_m,[3,53] valence electron concentration (VEC),[3,55,56] atomic-size difference δ,[3,53,57] entropy of mixing, ΔS_{mix},[3,57] Ω (the ratio of ΔS_{mix} to ΔH_{mix})[3,53,57,62,63], and enthalpy of mixing, ΔH_{mix}.[3,54,57,62,63] In the present work, the δ, Ω, and VEC of our present HEA were investigated.

δ can be obtained by eqn (1)[3,53,57,62,63]

$$\delta = \sqrt{\sum_{i=1}^{n} c_i \left(1 - \frac{r_i}{\sum_{i=1}^{n}(c_i r_i)}\right)^2}, \quad (1)$$

where c_i and r_i represent the atomic percentage and the atomic radius of the ith component, respectively. Based on eqn (1), the calculated δ of the CoCrCuMnNi HEA is 4.3%.

Ω can be derived by eqn (2)–(5)[3,53,54,57,62,63]

$$\Omega = \frac{T_m \Delta S_{mix}}{|\Delta H_{mix}|} \quad (2)$$

$$T_m = \sum_{i=1}^{n}(c_i (T_m)_i) \quad (3)$$

$$\Delta S_{mix} = -R\sum_{i=1}^{n}(c_i \ln c_i) \quad (4)$$

$$\Delta H_{mix} = \sum_{i=1}^{n} \Omega_{ij} c_i c_{j i \neq j} \quad (5)$$

The number of component elements is represented by n. $(T_m)_i$ is the melting point of the ith constituent element, the universal gas constant, R, is 8.314 kJ^{-1} mol^{-1}, Ω_{ij} usually

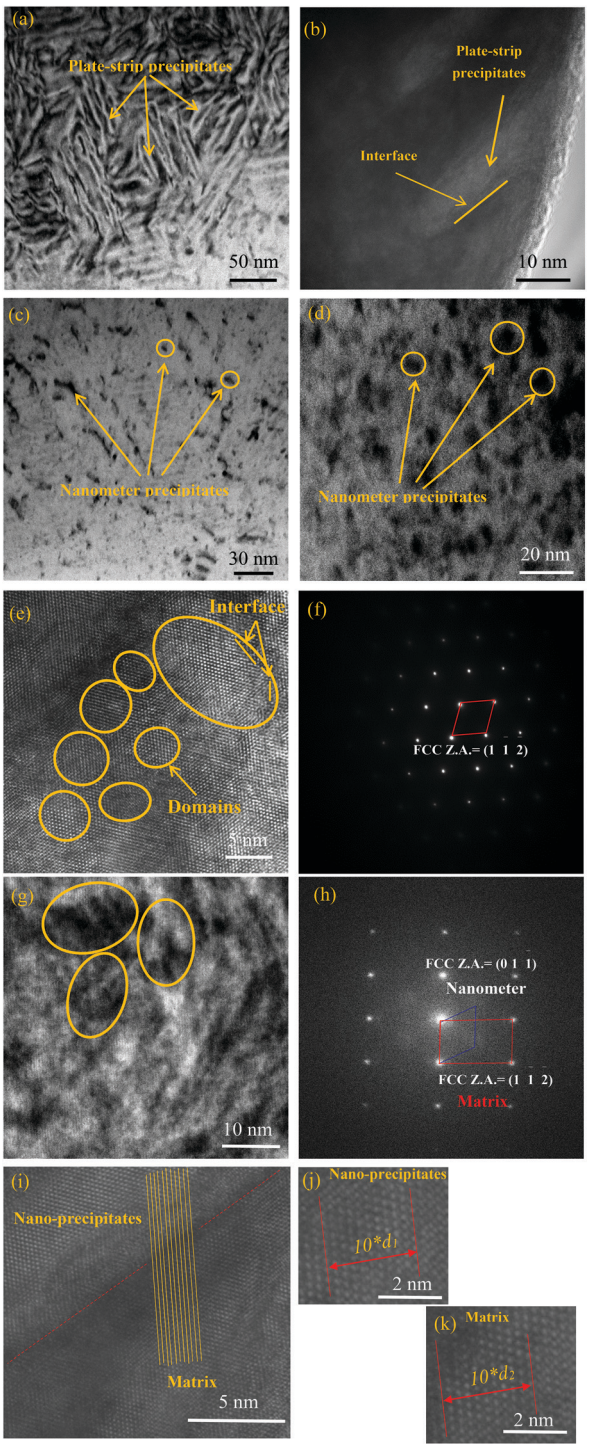

Fig. 5 TEM images of the CoCrCuMnNi high-entropy alloy. (a) Plate-strip precipitates in the HEA. (b) High-resolution TEM image showing the plate-strip precipitates. (c and d) Nanometer precipitates in the HEA. (e) High-resolution TEM image of the dendrite zone. (f) The corresponding selected-area diffraction (SAD) pattern for c. (g) Nanometer precipitates in the HEA. (h) The corresponding SAD pattern for g. (i) High-Resolution Transmission Electron Microscopy (HRTEM) image of this HEA, showing the details between the matrix and nano-precipitate interface. (j and k) HRTEM image of the nanometer precipitate and matrix.

equals 4 $\Delta H_{ij}^{\mathrm{mix}}$, and $\Delta H_{ij}^{\mathrm{mix}}$ represents the enthalpy of mixing between the ith and jth component elements. The values of $\Delta H_{ij}^{\mathrm{mix}}$ are displayed in Table 2.[3,54] Based on eqn (2)–(5), the obtained T_{m}, ΔS_{mix}, ΔH_{mix}, and Ω of the CoCrCuMnNi HEA are 1706.5 K, 13.38 kJ^{-1} mol^{-1}, 0.64 kJ mol^{-1}, and 35.68, respectively.

Previously, it was suggested that a stable solid-solution phase is formed in multi-component HEA systems[54] when $\Omega \geq 1.1$ and $\delta \leq 6.6\%$. Based on our calculated data, the CoCrCuMnNi HEA should form a stable solid-solution phase. However, two similar phases were observed in this HEA by XRD and SEM. Although the two phases possess an FCC structure, their elemental compositions are different. This phenomenon is caused by solute segregation.

VEC is described as[55,56,56,57]

$$\mathrm{VEC} = \sum_{i=1}^{n} c_i (\mathrm{VEC})_i \qquad (6)$$

where c_i and n are the atomic percentage of the ith component element and the number of component elements, respectively. The VEC of the ith component element is denoted by $(\mathrm{VEC})_i$. Based on eqn (6), the calculated VEC of the CoCrCuMnNi HEA is 8.2.

It was reported that a single FCC solid-solution phase should be formed with the VEC $\geq$ 8.[55,57] Both the FCC and BCC phases coexist[55,56] when 6.87 $\leq$ VEC $<$ 8. A single BCC phase is presented when VEC $<$ 6.87.[55,56] Alloys with a VEC between 6.88 and 7.84 are prone to the σ-phase formation either in the as-cast state or during aging at suitable temperatures.[58,59] The CoCrCuMnNi HEA, prepared by arc melting in the present work, satisfies the condition for forming a stable single FCC solid-solution structure based on the calculated data. However, the experimental results show that the CoCrCuMnNi HEA contains two similar FCC structures, which could be caused by the lattice-distortion difference produced by elemental segregation.

Based on the analysis results of TEM and EDS, the forming process of nanometer precipitates was established, as shown in Fig. 7. As the temperature decreases, the dendrites grow gradually, as presented in Fig. 7a and b. Fig. 7c shows that many nanometer precipitates are generated in the inter-dendrite zone. Fig. 7d shows that many nanometer precipitates are generated in the dendrite zone.

Three factors contribute to the formation of the nano-precipitates. Firstly, the atomic-diffusion velocity is reduced due to the sluggish diffusion effect in the HEA when a variety of elements are mixed together, which lowers the grain-growth speed, and provides time for nucleation. Secondly, the excessive Cu atoms gather in the inter-dendrite zone, which makes it easier for the segregation of Cu as cores with decreasing the temperature. This trend also promotes the formation of nanometer precipitates. Thirdly, as shown in Fig. 8, the ΔH_{mix} between Cu and Co, Cr, Mn, or Ni in the CoCrCuMnNi HEA is higher than that between any two of Co, Cr, Mn, and Ni elements, which leads to the separation of Cu from the

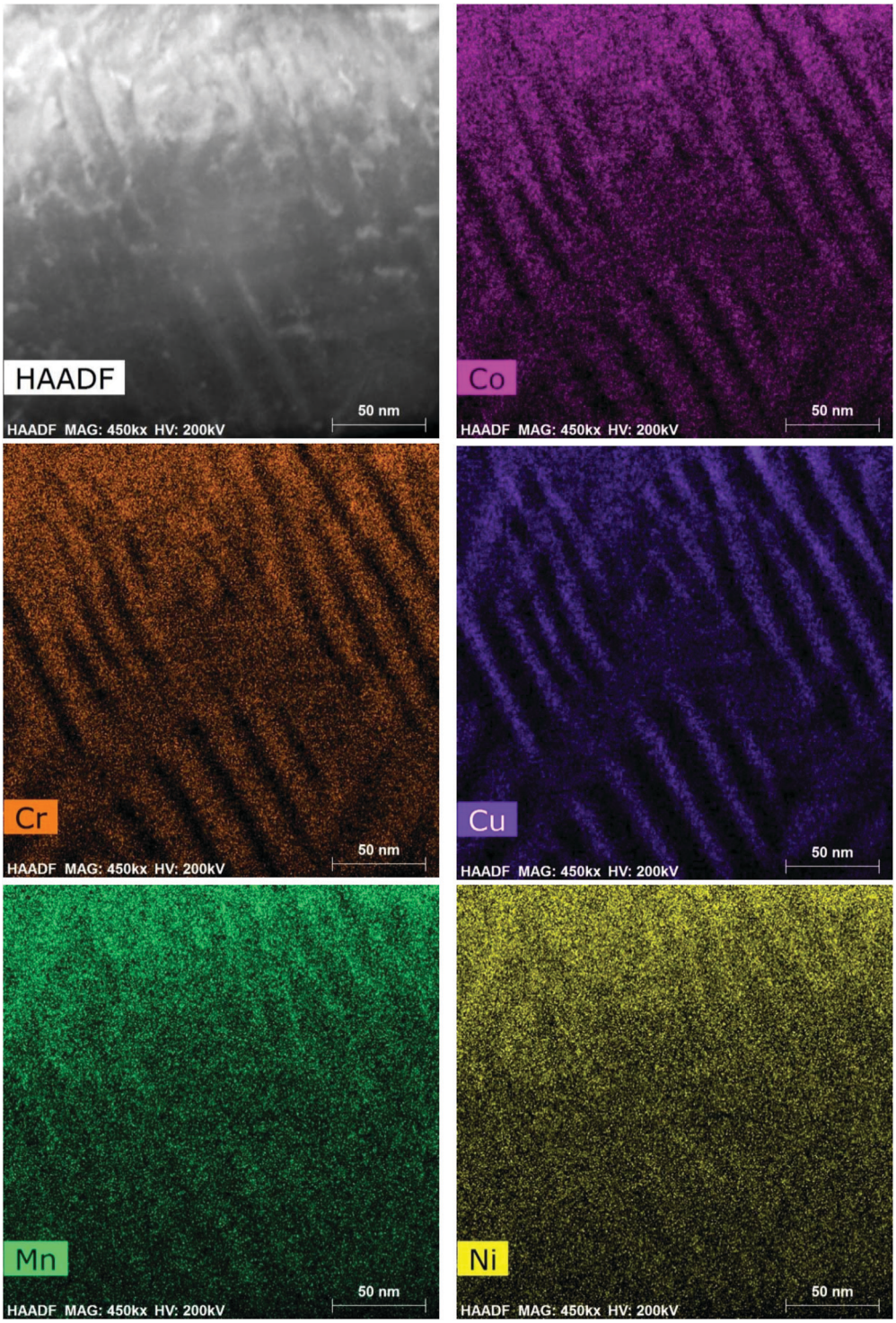

Fig. 6 Elemental distributions of the plate-strip precipitates in the CoCrCuMnNi HEA.

CoCrCuMnNi HEA, forming precipitates. It is difficult for the precipitates to increase in size due to the sluggish diffusion effect. Hence, the nanometer precipitates are formed.

In order to describe the formation process of nanometer precipitates in more detail, an atomic-diffusion model is proposed. As shown in Fig. 9a, Co, Cr, Cu, Mn, and Ni are mixed together when the alloy is in the liquid state. As the temperature decreases, the Cr, Co, Ni, and Mn are separated out, which is due to their higher melting point than that of Cu (see Fig. 9b). Then, a part of the Cu atoms dissolves in the CoCrMnNi matrix, forming the FCC1 (Co and Cr rich) phase. A part of the Cr, Co, Ni, and Mn atoms dissolve in the Cu matrix,

Table 2 Enthalpy of mixing (ΔH_{ij}^{mix}, kJ mol^{-1}) in binary equi-atomic alloys

Element (atomic radius, nm)	Co	Cr	Cu	Mn	Ni
Co (0.1251)	—	−4	6	−5	0
Cr (0.1249)	−4	—	12	2	−7
Cu (0.1278)	6	12	—	4	4
Mn (0.1350)	−5	2	4	—	−8
Ni (0.1246)	0	−7	4	−8	—

forming the FCC2 (Cu rich) phase (see Fig. 9c). Furthermore, some Cr, Co, Ni, and Mn atoms are separated out from the (Cr, Co, Ni and Mn)-supersaturated solid solution, while the rest of the Cu atoms are separated out from the Cu-supersaturated solid-solution, forming precipitates (see Fig. 9d).

The basic reinforcement mechanism for materials contains solid-solution strengthening,[65–69] strain hardening,[26,69] phase-transformation strengthening,[26,70,71] fine-grain strengthening,[6,21] and second-phase strengthening.[26,65–69] The second-phase strengthening and solid-solution strengthening are analyzed in our as-cast CoCrCuMnNi HEA. Our proposed HEA (CoCrCuMnNi) contains five elements with very different atomic radii, which will cause a larger lattice distortion and contribute to the solid-solution strengthening. Furthermore, in our HEA (CoCrCuMnNi), a large amount of nanometer-precipitates and domains were observed, which hinders the dislocation movement and further contributes to the improvement of strength.

To evaluate the solid-solution-strengthening effect on our proposed HEA, we investigated the Labusch-strengthening factor proposed by Wu *et al.*[72,73] To compare the solid-solution-strengthening effects, we calculated the Labusch-strengthening factors, ($L_{CoCrMnNi \rightarrow CoCrFeMnNi}$ and $L_{CoCrMnNi \rightarrow CoCrCuMnNi}$)

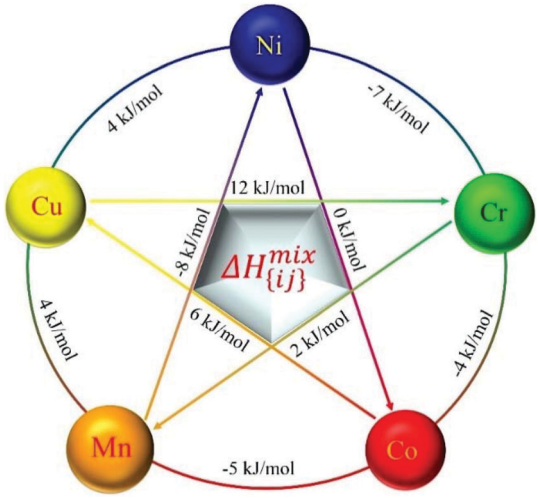

Fig. 8 ΔH_{mix} (enthalpy of mixing) between any two elements in the CoCrCuMnNi HEA.

for the CoCrFeMnNi and CoCrCuMnNi HEAs, respectively, by eqn (7)

$$L_{M\rightarrow N} = \mu_N \left\{ \sum_{i=M+1}^{N} \left[\left(\frac{\eta_i}{1+\frac{1}{2}\eta_i} \right)^2 + \alpha^2 {\delta_i}^2 \right] x_i \right\}^{\frac{2}{3}}, \quad (7)$$

where μ_N is the shear modulus of the N-element alloy, x_i is the molar fraction of the ith element, and α is a dimensionless parameter.[72,73] η_i and δ_i are the modulus and lattice mismatches, and they can be obtained by

$$\eta_i = \frac{1}{\mu}\frac{d\mu_i}{dx_i}, \ \delta_i = \frac{1}{a}\frac{da_i}{dx_i}, \quad (8)$$

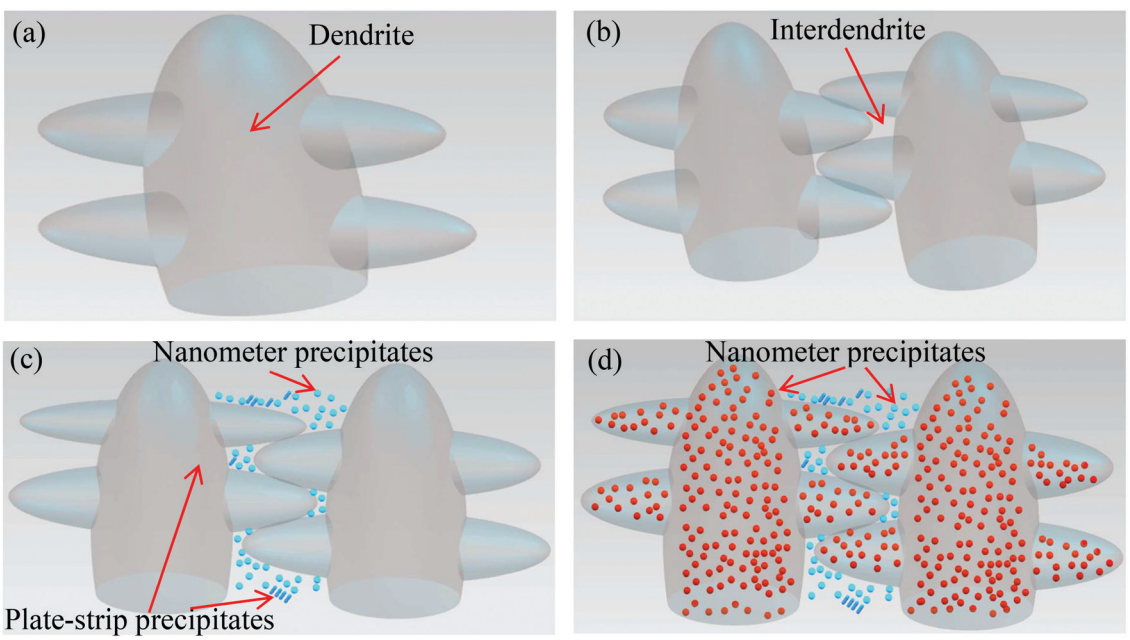

Fig. 7 Schematic diagram of the nanometer-precipitate-forming process.

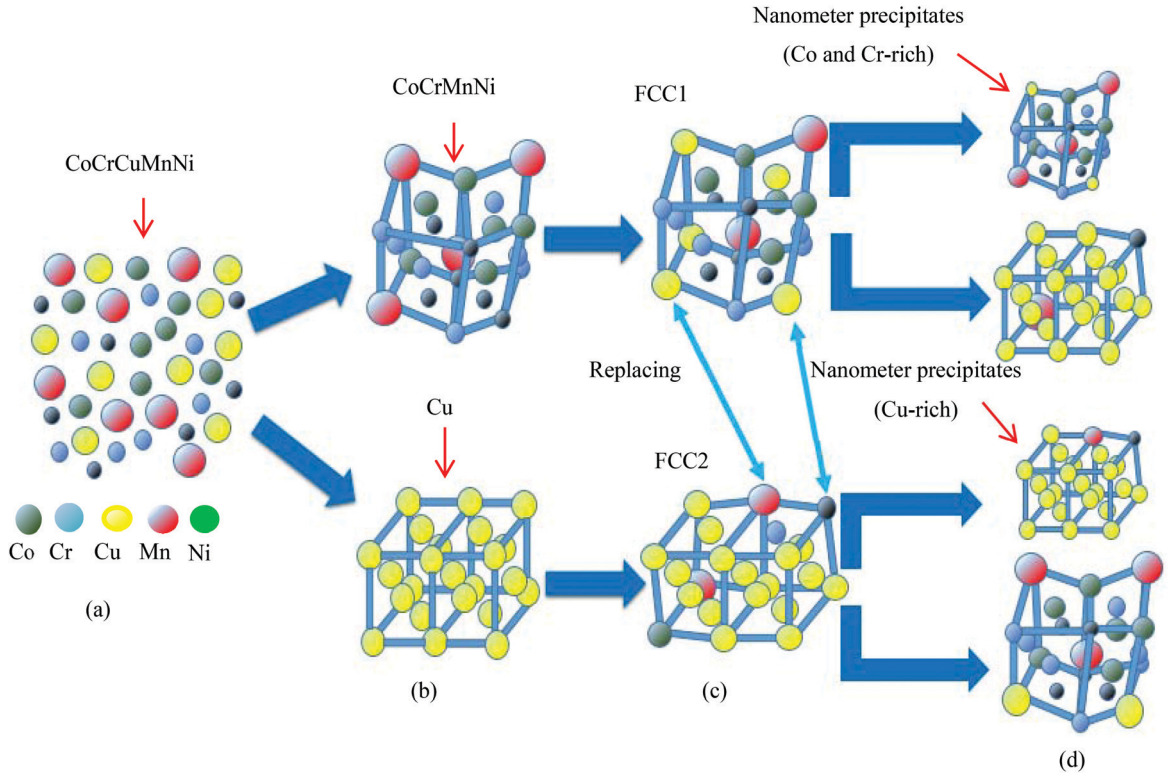

Fig. 9 Atomic-diffusion model for the forming process of nanometer precipitates.

where $a(\mu)$ and $a_i(\mu_i)$ are the lattice constants (shear modulus) of the alloy and the solute element, respectively.

Assuming a linear relationship between the lattice constants and shear moduli of equiatomic alloys and their constituent elements, a_{Cu} and μ_{Cu} can be derived from eqn (9)–(12)

$$\left(\frac{4}{5}a_{CoCrMnNi} + \frac{1}{5}a_{Cu}\right) = a_{CoCrCuMnNi} \quad (9)$$

$$\left(\frac{4}{5}\mu_{CoCrMnNi} + \frac{1}{5}\mu_{Cu}\right) = \mu_{CoCrCuMnNi} \quad (10)$$

$$\left(\frac{4}{5}a_{CoCrMnNi} + \frac{1}{5}a_{Fe}\right) = a_{CoCrFeMnNi} \quad (11)$$

$$\left(\frac{4}{5}\mu_{CoCrMnNi} + \frac{1}{5}\mu_{Fe}\right) = \mu_{CoCrFeMnNi}. \quad (12)$$

where $a_{CoCrCuMnNi}$ and $\mu_{CoCrCuMnNi}$ were obtained from the XRD and tensile test; $a_{CoCrFeMnNi}$, $\mu_{CoCrFeMnNi}$, a_{Fe} and μ_{Fe} were adopted from the previous study.[72,73]

Based on eqn (8), η_{Cu}, δ_{Cu}, η_{Fe} and δ_{Fe} can be derived from eqn (13)–(16)

$$\eta_{Cu} = \frac{\mu_{Cu} - \mu_{CoCrCuMnNi}}{(1 - x_{Cu})\mu_{CoCrCuMnNi}} \quad (13)$$

$$\delta_{Cu} = \frac{a_{Cu} - a_{CoCrCuMnNi}}{(1 - x_{Cu})a_{CoCrCuMnNi}} \quad (14)$$

$$\eta_{Fe} = \frac{\mu_{Fe} - \mu_{CoCrFeMnNi}}{(1 - x_{Fe})\mu_{CoCrFeMnNi}} \quad (15)$$

$$\delta_{Fe} = \frac{a_{Fe} - a_{CoCrFeMnNi}}{(1 - x_{Fe})a_{CoCrFeMnNi}}. \quad (16)$$

Using the obtained data, the Labusch-strengthening factors of $L_{CoCrMnNi \rightarrow CoCrFeMnNi}$ (from CoCrMnNi to CoCrMnNi + Fe) and $L_{CoCrMnNi \rightarrow CoCrCuMnNi}$ (CoCrMnNi to CoCrMnNi + Cu) were calculated to be 6.29 and 7.9, respectively, based on eqn (7). This result indicates that Cu has a higher solid-solution strengthening effect than Fe on CoCrMnNi.

In order to conduct the quantitative analysis of the solid-solution strengthening by introducing Cu, we evaluated the solid-solution strength by a conventional formula[74,75]

$$\Delta\sigma_s = \frac{MGC^{\frac{1}{2}}\left|\frac{\varepsilon_G}{1 + 0.5|\varepsilon_G|} - 3\varepsilon_a\right|^{\frac{3}{2}}}{700}. \quad (17)$$

Here C and G are the concentration and shear modulus of solute elements, respectively. M[76] is the Taylor factor, which is 3.06. We treated the CoCrCuMnNi HEA as a pseudo-binary alloy, $X_{0.8}Cu_{0.2}$ (X denotes the CoCrMnNi HEA). Using the above obtained ε_G, η_{Cu}, ε_a, and δ_{Cu}, the obtained value of $\Delta\sigma_s$ is 39 MPa by adding Cu into the CoCrMnNi HEA. Using the same method, the calculated value of $\Delta\sigma_s$ is 10 MPa by adding Fe into the CoCrMnNi HEA. These results further demonstrate that the introduction of Cu has a higher solid-solution-

strengthening effect on CoCrMnNi than adding Fe. Moreover, this result implies that the appearance of the nanometer-precipitates and domains is the main strengthening mechanism for the CoCrCuMnNi HEA that has a yield strength of 458 MPa.

To summarize, we designed and prepared the CoCrCuMnNi HEA, which possesses a good comprehensive mechanical performance, *i.e.*, a yield strength of 458 MPa, and an ultimate tensile strength of 742 MPa with an elongation of 40%. We observed a large amount of nanometer precipitates (5–50 nm in size) and domains (5–10 nm in size) are generated in the CoCrCuMnNi HEA. The calculated results of the enthalpy of mixing show that Cu and Co, Cr, Mn, or Ni has a higher enthalpy of mixing, which promotes the separation of Cu-rich precipitates. It is difficult for the Cu-rich precipitates to grow because of the sluggish diffusion effect. Hence, the nanometer precipitates are formed. We compare the Labusch-strengthening factors ($L_{\mathrm{CoCrMnNi}\rightarrow\mathrm{CoCrFeMnNi}}$ and $L_{\mathrm{CoCrMnNi}\rightarrow\mathrm{CoCrCuMnNi}}$) for the CoCrFeMnNi and CoCrCuMnNi HEAs; this shows that Cu has a higher solid-solution strengthening effect than Fe on CoCrMnNi. We obtained the additional value of solid-solution strengthening produced by adding Cu, which is much smaller than the measurements obtained by the tension test. This trend indicates that nanometer-precipitate strengthening has a greater effect than the solid-solution-strengthening mechanism.

Conclusions

It should be emphasized that we have not only developed a CoCrCuMnNi HEA in the current work, but our study also sheds light on developing HEAs with remarkable mechanical properties. Furthermore, some main conclusions are drawn.

1. The CoCrCuMnNi HEA is composed of two FCC phases. A large amount of nanometer precipitates (5–50 nm in size) and domains (5–10 nm in size) are found in the inter-dendrite and dendrite zones.

2. This CoCrCuMnNi HEA prepared by vacuum arc melting exhibits excellent mechanical properties. The obtained tensile yield and the ultimate tensile strengths are about 458 MPa and 742 MPa, respectively, and the corresponding elongation is approximately 40%. This HEA has a mechanical response almost identical to those of the single-phase $Fe_{20}Mn_{20}Ni_{20}Co_{20}Cr_{20}$ HEA (grain-refined) and the dual-phase $Fe_{50}Mn_{30}Co_{10}Cr_{10}$ HEA (as-homogenized), the two most successful HEAs to date.

3. The enthalpy of mixing between Cu and Co, Cr, Mn, or Ni is higher than that between any two of Cr, Co, Ni, and Mn elements, which is the key factor for the separation of Cu from the CoCrCuMnNi HEA.

4. The second-phase-strengthening mechanism plays an important role in the strengthening of the CoCrCuMnNi HEA.

Conflicts of interest

There are no conflicts to declare.

Acknowledgements

The authors acknowledge the support from the Fund of the State Key Laboratory of Advanced Welding and Joining, and the National Natural Science Foundation of China for Distinguished Young Scientists (No. 51825401). Xiaoqing Li acknowledges the support from the Swedish Research Council and the Swedish National Infrastructure for Computing (SNIC) at the National Supercomputer Centre in Linköping. Peter K. Liaw is very grateful to the support of (1) the National Science Foundation (DMR-1611180 and 1809640) with the program directors, Drs. G. Shiflet and D. Farkas and (2) the U. S. Army Research Office project (W911NF-13-1-0438 and W911NF-19-2-0049) with the program managers, Drs. M. P. Bakas, S. N. Mathaudhu, and D. M. Stepp. Gang Qin very much appreciates the support of the China Scholarship Council.

References

1 Y. P. Lu, X. X. Gao, Y. Dong, T. M. Wang, H. L. Chen, H. H. Mao, Y. H. Zhao, H. Jiang, Z. Q. Cao, T. J. Li and S. Guo, Preparing bulk ultrafine-microstructure high-entropy alloys via direct solidification, *Nanoscale*, 2018, **10**, 1912–1919.

2 M. C. Gao, J. W. Yeh, P. K. Liaw and Y. Zhang, *High-Entropy Alloys*, Springer International Publishing, 2016.

3 Y. Zhang, T. T. Zuo, Z. Tang, M. C. Gao, K. Dahmen, P. K. Liaw and Z. P. Lu, Microstructures and properties of high-entropy alloys, *Prog. Mater. Sci.*, 2014, **61**, 1–93.

4 X. Q. Li, S. Schönecker, W. Li, L. K. Varga, D. L. Irving and L. Vitos, Tensile and shear loading of four fcc high-entropy alloys: a first-principle study, *Phys. Rev. B*, 2018, **97**, 094102.

5 G. Qin, R. R. Chen, H. T. Zheng, H. Z. Fang, L. Wang, Y. Q. Su, J. J. Guo and H. Z. Fu, FCC-CoCrFeMnNi high entropy alloys by Mo addition, *J. Mater. Sci. Technol.*, 2019, **35**, 578–583.

6 S. J. Sun, Y. Z. Tian, H. R. Lin, X. G. Dong, Y. H. Wang, Z. J. Zhang and Z. F. Zhang, Enhanced strength and ductility of bulk CoCrFeMnNi high entropy alloy having fully recrystallized ultrafine-grained structure, *Mater. Des.*, 2017, **133**, 122–127.

7 Y. P. Lu, Y. Dong, S. Guo, L. Jiang, H. J. Kang, T. M. Wang, B. Wen, Z. J. Wang, J. C. Jie, Z. Q. Cao, H. H. Ruan and T. J. Li, A promising new class of high-temperature alloys: Eutectic high-entropy alloys, *Sci. Rep.*, 2014, **4**, 6200.

8 Y. Zhang, Y. Liu, Y. X. Li, X. Chen and H. W. Zhang, Microstructure and mechanical properties of a refractory HfNbTiVSi0.5 high-entropy alloy composite, *Mater. Lett.*, 2016, **174**, 82–85.

9 Y. Liu, Y. Zhang, H. Zhang, N. J. Wang, X. Chen, H. W. Zhang and Y. X. Li, Microstructure and mechanical properties of refractory HfMo0.5NbTiV0.5Six high-entropy composites, *J. Alloys Compd.*, 2017, **694**, 869–876.

10 D. X. Wei, X. Q. Li, S. Schönecker, J. Jiang, W. M. Choi, B. J. Lee, H. S. Kim, A. Chiba and H. Kato, Development of strong and ductile metastable face-centered cubic single-phase high-entropy alloys, *Acta Mater.*, 2019, **181**, 318–330.

11 C. L. Tracy, S. Park, D. R. Rittman, S. J. Zinkle, H. Bei, M. Lang, R. C. Ewing and W. L. Mao, High pressure synthesis of a hexagonal close-packed phase of the high-entropy alloy CrMnFeCoNi, *Nat. Commun.*, 2017, **8**, 15634.

12 G. Qin, S. Wang, R. R. Chen, X. Gong, L. Wang, Y. Q. Su, J. J. Guo and H. Z. Fu, Microstructures and mechanical properties of Nb-alloyed CoCrCuFeNi high-entropy alloys, *J. Mater. Sci. Technol.*, 2018, **34**, 365–369.

13 Z. J. Zhang, M. M. Mao, J. Wang, B. Gludovatz, Z. Zhang, S. X. Mao, E. P. George, Q. Yu and R. O. Ritchie, Nanoscale origins of the damage tolerance of the high-entropy alloy CrMnFeCoNi, *Nat. Commun.*, 2015, **6**, 10143.

14 X. B. Feng, J. Y. Zhang, K. Wu, X. Q. Liang, G. Liu and J. Sun, Ultrastrong Al0.1CoCrFeNi high-entropy alloys at small scales: effects of stacking faults vs. nanotwins, *Nanoscale*, 2018, **10**, 13329.

15 Z. Y. Rao, X. Wang, J. Zhu, X. H. Chen, L. Wang, J. J. Si, Y. D. Wu and X. D. Hui, Affordable FeCrNiMnCu high entropy alloys with excellent comprehensive tensile properties, *Intermetallics*, 2016, **77**, 23–33.

16 Y. P. Lu, X. Z. Gao, L. Jiang, Z. N. Chen, T. M. Wang, J. C. Jie, H. J. Kang, Y. B. Zhang, S. Guo, H. H. Ruan, Y. H. Zhao, Z. Q. Cao and T. J. Li, Directly cast bulk eutectic and near-eutectic high entropy alloys with balanced strength and ductility in a wide temperature range, *Acta Mater.*, 2017, **124**, 143–150.

17 Y. Ma, C. Li, L. Santodonato, M. Feygenson, C. Dong and P. K. Liaw, Chemical short-range orders and the induced structural transition in high-entropy alloys, *Scr. Mater.*, 2018, **144**, 64–68.

18 X. Jin, Y. Zhou, L. Zhang, X. Y. Du and B. S. Li, A new pseudo binary strategy to design eutectic high entropy alloys using mixing enthalpy and valence electron concentration, *Mater. Des.*, 2018, **143**, 49–55.

19 L. Zhang, Y. Zhou, X. Jin, X. Y. Du and B. S. Li, The microstructure and high-temperature properties of novel nano precipitation-hardened face centered cubic high-entropy superalloys, *Scr. Mater.*, 2018, **146**, 226–230.

20 Z. Fu, B. E. MacDonald, D. Zhang, B. Wu, W. Chen, J. Ivanisenko, H. Hahn and E. J. Lavernia, Fcc nanostructured TiFeCoNi alloy with multi-scale grains and enhanced plasticity, *Scr. Mater.*, 2018, **143**, 108–112.

21 S. J. Sun, Y. Z. Tian, H. R. Lin, H. J. Yang, X. G. Dong, Y. H. Wang and Z. F. Zhang, Transition of twinning behavior in the CoCrFeMnNi high entropy alloy with grain refinement, *Mater. Sci. Eng., A*, 2018, **712**, 603–607.

22 Y. Ma, Q. Wang, B. B. Jiang, C. L. Li, J. M. Hao, X. N. Li, C. Dong and T. G. Nieh, Controlled formation of coherent cuboidal nanoprecipitates in body-centered cubic high-entropy alloys based on Al2 (Ni, Co, Fe, Cr) 14 compositions, *Acta Mater.*, 2018, **147**, 213–225.

23 N. Gao, D. H. Lu, Y. Y. Zhao, X. W. Liu, G. H. Liu, Y. Wu, G. Liu, Z. T. Fan, Z. P. Lu and E. P. George, Strengthening of a CrMnFeCoNi high-entropy alloy by carbide precipitation, *J. Alloys Compd.*, 2019, **792**, 1028–1035.

24 J. W. Yeh, S. K. Chen, S. J. Lin, J. Y. Gan, T. S. Chin, T. T. Shun, C. H. Tsau and S. Y. Chang, Nanostructured high-entropy alloys with multiple principal elements: novel alloy design concepts and outcomes, *Adv. Eng. Mater.*, 2004, **6**, 299–303.

25 B. Cantor, I. T. H. Chang, P. Knight and A. J. B. Vincent, Microstructural development in equiatomic multicomponent alloys, *Mater. Sci. Eng., A*, 2004, **375**, 213–218.

26 Z. M. Li, G. P. Konda, D. Yun, R. Dierk and C. C. Tasan, Metastable high-entropy dual-phase alloys overcome the strength–ductility trade-off, *Nature*, 2016, **534**, 227–230.

27 Y. Zhang, T. Zuo, Y. Cheng and P. K. Liaw, High-entropy alloys with high saturation magnetization, electrical resistivity, and malleability, *Sci. Rep.*, 2013, **3**, 1455.

28 R. R. Chen, G. Qin, H. T. Zheng, L. Wang, Y. Q. Su, Y. L. Chiu, H. S. Ding, J. J. Guo and H. Z. Fu, Composition design of high entropy alloys using the valence electron concentration to balance strength and ductility, *Acta Mater.*, 2018, **144**, 129–137.

29 D. Li, C. Li, T. Feng, Y. Zhang, G. Sha, J. J. Lewandowski, P. K. Liaw and Y. Zhang, High-entropy Al0. 3CoCrFeNi alloy fibers with high tensile strength and ductility at ambient and cryogenic temperatures, *Acta Mater.*, 2017, **123**, 285–294.

30 T. Zuo, M. C. Gao, L. Ouyang, X. Yang, Y. Cheng, R. Feng, S. Y. Chen, P. K. Liaw, J. A. Hawk and Y. Zhang, Tailoring magnetic behavior of CoFeMnNiX (X=Al, Cr, Ga, and Sn) high entropy alloys by metal doping, *Acta Mater.*, 2017, **130**, 10–18.

31 T. Zuo, M. C. Gao, L. Ouyang, X. Yang, Y. Cheng, R. Feng, S. Y. Chen, P. K. Liaw, J. A. Hawk and Y. Zhang, The high-entropy alloys with high hardness and soft magnetic property prepared by mechanical alloying and high-pressure sintering, *Intermetallics*, 2016, **70**, 82–87.

32 T. Yang, Y. L. Zhao, Y. Tong, Z. B. Jiao, J. Wei, J. X. Cai, X. D. Han, D. Chen, A. Hu, J. J. Kai, K. Lu, Y. Liu and C. T. Liu, Multicomponent intermetallic nanoparticles and superb mechanical behaviors of complex alloys, *Science*, 2018, **362**, 933–937.

33 B. Ren, Z. X. Liu, D. M. Li, L. Shi, B. Cai and M. X. Wang, Effect of elemental interaction on the microstructure of the CuCrFeNiMn high entropy alloy system, *J. Alloys Compd.*, 2010, **493**, 148–153.

34 A. Marshal, K. G. Pradeep, D. Music, S. Zaefferer, P. S. De and J. M. Schneider, Combinatorial synthesis of high entropy alloys: Introduction of a novel, single phase, body-centered-cubic FeMnCoCrAl solid solution, *J. Alloys Compd.*, 2016, **691**, 683–689.

35 N. N. Guo, L. Wang, L. S. Luo, X. Z. Li, Y. Q. Su, J. J. Guo and H. Z. Fu, Microstructure and mechanical properties of refractory MoNbHfZrTi high-entropy alloys, *Mater. Des.*, 2015, **81**, 87–94.

36 S. Sohn, Y. Liu, J. Liu, P. Gong, S. Prades-Rodel, A. Blatter, B. E. Scanley, C. C. Broadbridge and J. Schroers, Noble metal high entropy alloys, *Scr. Mater.*, 2017, **126**, 29–32.

37 Z. Fu, W. Chen, H. Wen, D. Zhang, Z. Chen, B. Zheng, Y. Zhou and E. Lavernia, Microstructure and strengthening mechanisms in an FCC structured single-phase nanocrystalline $Co_{25}Ni_{25}Fe_{25}Al_{7.5}Cu_{17.5}$ high-entropy alloy, *Acta Mater.*, 2016, **107**, 59–71.

38 J. B. Cheng, X. B. Liang, Z. H. Wang and B. S. Xu, Formation and mechanical properties of CoNiCuFeCr high-entropy alloy coatings prepared by the plasma transferred arc cladding process, *Plasma Chem. Plasma Process.*, 2013, **33**, 979–992.

39 H. Zhang, Y. Pan and Y. Z. He, Synthesis and characterization of FeCoNiCrCu high-entropy alloy coating by laser cladding, *Mater. Des.*, 2011, **32**, 1910–1915.

40 G. X. Ye, B. Wu, C. H. Zhang, T. Chen, M. H. Lin, Y. J. Xie, Y. X. Xiao, W. J. Zhang, L. K. Zhang, Z. H. Zheng and C. Wang, Study of solidification microstructures of multi-principal high-entropy alloy FeCoNiCrMn by using experiments and simulation, *Adv. Mater. Res.*, 2012, **399**, 1746–1749.

41 P. P. Bhattacharjee, G. D. Sathiaraj, M. Zaid, J. R. Gatti, C. Lee, C. W. Tsai and J. W. Yeh, Microstructure and texture evolution during annealing of equiatomic CoCrFeMnNi high-entropy alloys, *J. Alloys Compd.*, 2014, **587**, 544–552.

42 T. A, N. P. Gurao and K. Biswas, In the quest of single phase multi-component multiprincipal high entropy alloys, *J. Alloys Compd.*, 2016, **697**, 432–442.

43 G. Qin, W. T. Xue, C. L. Fan, R. R. Chen, L. Wang, Y. Q. Su, H. S. Ding and J. J. Guo, Effect of Co content on phase formation and mechanical properties of $(AlCoCrFeNi)_{100-x}Co_x$ high-entropy alloys, *Mater. Sci. Eng., A*, 2018, **710**, 200–205.

44 F. Otto, Y. Yang, H. Bei and E. P. George, Relative effects of enthalpy and entropy on the phase stability of equiatomic high-entropy alloys, *Acta Mater.*, 2013, **61**, 2628–2638.

45 Y. Deng, C. C. Tasan, K. G. Pradeep, H. Springer, A. Kostka and D. Raabe, Design of a twinning-induced plasticity high entropy alloy, *Acta Mater.*, 2015, **94**, 124–133.

46 W. H. Liu, Z. P. Lu, J. Y. He, J. H. Luan, Z. J. Wang, B. Liu, Y. Liu and M. W. Chen, Ductile CoCrFeNiMox high entropy alloys strengthened by hard intermetallic phases, *Acta Mater.*, 2016, **116**, 332–342.

47 W. H. Liu, J. Y. He, H. L. Huang, H. Wang, Z. P. Lu and C. T. Liu, Effects of Nb additions on the microstructure and mechanical property of CoCrFeNi high-entropy alloys, *Intermetallics*, 2015, **60**, 1–8.

48 J. Y. He, W. H. Liu, H. Wang, Y. Wu, X. J. Liu, T. G. Nieh and Z. P. Lu, Effects of Al addition on structural evolution and tensile properties of the FeCoNiCrMn high-entropy alloy system, *Acta Mater.*, 2014, **62**, 105–113.

49 B. Gludovatz, A. Hohenwarter, D. Catoor, E. H. Chang, E. P. George and R. O. Ritchie, A fracture-resistant high-entropy alloy for cryogenic applications, *Science*, 2014, **345**, 1153–1158.

50 X. Jin, Y. Zhou, L. Zhang, X. Y. Du and B. S. Li, novel Fe20Co20Ni41Al19 eutectic high entropy alloy with excellent tensile properties, *Mater. Lett.*, 2018, **216**, 144–146.

51 T. Bhattacharjee, R. X. Zheng, Y. Chong, S. Sheikh, S. Guo, I. T. Clark, T. Okawa, I. S. Wani, P. P. Bhattacharjee, A. Shibata and N. Tsuji, Effect of low temperature on tensile properties of the AlCoCrFeNi2.1eutectic high entropy alloy, *Mater. Chem. Phys.*, 2018, **210**, 207–212.

52 G. Qin, R. R. Chen, P. K. Liaw, Y. F. Gao, X. Q. Li, H. T. Zheng, L. Wang, Y. Q. Su, J. J. Guo and H. Z. Fu, A novel face-centered-cubic high-entropy alloy strengthened by nanoscale precipitates, *Scr. Mater.*, 2019, **172**, 51–55.

53 X. Yang and Y. Zhang, Prediction of high-entropy stabilized solid-solution in multi-component alloys, *Mater. Chem. Phys.*, 2012, **132**, 233–238.

54 A. Takeuchi and A. Inoue, Classification of bulk metallic glasses by atomic size difference, heat of mixing and period of constituent elements and its application to characterization of the main alloying element, *Mater. Trans.*, 2006, **46**, 2817–2829.

55 S. Guo, C. Ng, J. Lu and C. T. Liu, Effect of valence electron concentration on stability of the fcc or bcc phase in high entropy alloys, *J. Appl. Phys.*, 2011, **109**, 645–647.

56 S. Guo and C. T. Liu, Phase stability in high entropy alloys: Formation of the solid-solution phase or amorphous phase, *Prog. Nat. Sci.*, 2011, **21**, 433–446.

57 Y. Zhang, Y. Zhou, J. Lin, G. Chen and P. K. Liaw, SolidSolution Phase Formation Rules for Multi-component Alloys, *Adv. Eng. Mater.*, 2008, **10**, 534–538.

58 M. H. Tsai, K. Y. Tsai, C. W. Tsai, C. Lee, C. C. Juan and J. W. Ye, Criterion for Sigma Phase Formation in Cr- and V-Containing High-Entropy Alloys, *Mater. Res. Lett.*, 2013, **1**, 207–212.

59 M. H. Tsai, K. C. Chang, J. H. Li, R. C. Tsai and A. H. Cheng, A second criterion for sigma phase formation in high-entropy alloys, *Mater. Res. Lett.*, 2016, **4**, 1–6.

60 M. C. Troparevsky, J. R. Morris, P. R. C. Kent, A. R. Lupini and G. M. Stocks, Criteria for Predicting the Formation of Single-Phase High-Entropy Alloys, *Phys. Rev. X*, 2015, **5**, 1–6.

61 N. Yurchenko, N. Stepanov and G. Salishchev, Laves-phase formation criterion for high-entropy alloys, *Met. Sci. J.*, 2016, **33**, 17–22.

62 R. Feng, M. C. Gao, C. Lee, M. Mathes, T. T. Zuo, S. Y. Chen, J. A. Hawk, Y. Zhang and P. K. Liaw, Design of Light-weight high-entropy alloys, *Entropy*, 2016, **18**, 333.

63 Y. Zhang, Z. P. Lu, S. G. Ma, P. K. Liaw, Z. Tang, Y. Q. Cheng and M. C. Gao, Guidelines for predicting phase formation of high-entropy alloys, *MRS Commun.*, 2014, **42**, 57–62.

64 M. G. Poletti and L. Battezzati, Electronic and thermodynamic criteria for the occurrence of high entropy alloys in metallic systems, *Acta Mater.*, 2014, **75**, 297–306.

65 J. C. Rao, H. Y. Diao, V. Ocelík, D. Vainchtein, C. Zhang, C. Kuo, Z. Tang, W. Guo, J. D. Poplawsky, Y. Zhou, P. K. Liaw and J. Th. M. De Hosson, Secondary phases in AlxCoCrFeNi high-entropy alloys: An *in situ* TEM heating study and thermodynamic appraisal, *Acta Mater.*, 2017, **131**, 206–220.

66 I. Basu, V. Ocelík and J. Th. M. De Hosson, Size dependent plasticity and damage response in multiphase body centered cubic high entropy alloys, *Acta Mater.*, 2018, **150**, 104–116.
67 I. Basu, V. Ocelík and J. Th. M. De Hosson, BCC-FCC interfacial effects on plasticity and strengthening mechanisms in high entropy alloys, *Acta Mater.*, 2018, **157**, 83–95.
68 I. Basu, V. Ocelík and J. Th. M. De Hosson, Size effects on plasticity in high-entropy alloys, *J. Mater. Res.*, 2018, **33**, 3055–3076.
69 Y. P. Cai, G. J. Wang, Y. J. Ma, Z. H. Cao and X. K. Meng, High hardness dual-phase high entropy alloy thin films produced by interface alloying, *Scr. Mater.*, 2019, **162**, 281–285.
70 D. X. Wei, X. Q. Li, J. Jiang, W. C. Heng, Y. C. Koizumi, W. M. Choi, B. J. Lee, H. S. Kim, H. Kato and A. Chiba, Novel Co-rich high performance twinning-induced plasticity (TWIP) and transformation-induced plasticity (TRIP) high-entropy alloys, *Scr. Mater.*, 2019, **165**, 39–43.
71 D. X. Wei, X. Q. Li, W. C. Heng, Y. C. Koizumi, F. He, W. Choi, B. J. Lee, H. S. Kim, H. Kato and A. Chiba, Novel Co-rich high entropy alloys with superior tensile properties, *Mater. Res. Lett.*, 2019, **7**, 82–88.
72 Z. G. Wu, Y. F. Gao and H. B. Bei, Thermal activation mechanisms and Labusch-type strengthening analysis for a family of high-entropy and equiatomic solid-solution alloys, *Acta Mater.*, 2016, **120**, 108–119.
73 Z. G. Wu, W. Guo, K. Jin, Y. F. Gao and H. B. Bei, Enhanced strength and ductility of a tungsten-doped CoCrNi medium-entropy alloy, *J. Mater. Res.*, 2018, **33**, 3301–3309.
74 R. L. Fleischer, Substitutional solution hardening, *Acta Metall.*, 1963, **11**, 203–209.
75 T. H. Courtney, *Mechanical behavior of materials*, McGraw-Hill, New York, 1990.
76 G. I. Taylor, The Mechanism of Plastic Deformation of Crystals. Part I. Theoretical, *Proc. R. Soc. London, Ser. A*, 1934, **145**, 362–387.
77 X. W. Liu, G. Laplanche, A. Kostka, S. G. Fries, J. Pfetzing-Micklich, G. Liu and E. P. George, Columnar to equiaxed transition and grain refinement of the cast CrCoNi medium-entropy alloy by microalloying with titanium and carbon, *J. Alloys Compd.*, 2019, **775**, 1068–1076.
78 H. Y. Diao, D. Ma, R. Feng, T. K. Liu, C. Pu, C. Zhang, W. Guo, J. D. Poplawsky, Y. F. Gao and P. K. Liaw, Novel NiAl-strengthened high entropy alloys with balanced tensile strength and ductility, *Mater. Sci. Eng., A*, 2019, **742**, 636–647.
79 C. W. Tsai, C. Lee, P. T. Lin, X. Xie, S. Y. Chen, R. Carroll, M. LeBlanc, B. A. W. Brinkman, P. K. Liaw, K. A. Dahmen and J. W. Yeh, Portevin-Le Chatelier mechanism in face-centered-cubic metallic alloys from low to high entropy, *Inter. J. P.*, 2019, **122**, 212–224.
80 J. Peng, Z. Y. Li, L. M. Fu, X. B. Ji, Z. R. Pang and A. D. Shan, Carbide precipitation strengthening in fine-grained carbon-doped FeCoCrNiMn high entropy alloys, *J. Alloys Compd.*, 2019, **803**, 491–498.
81 D. G. Kim, Y. H. Jo, J. M. Park, W. M. Choi, H. S. Kim, B. J. Lee, S. S. Sohn and S. Lee, Effects of annealing temperature on microstructures and tensile properties of a single FCC phase CoCuMnNi high-entropy alloy, *J. Alloys Compd.*, 2020, **812**, 152111.